Journal of Alloys and Compounds 513 (2012) 193–201

Contents lists available at SciVerse ScienceDirect

Journal of Alloys and Compounds

journal homepage: www.elsevier.com/locate/jallcom

Magnetic properties of carbon coated Fe, Co and Ni nanoparticles

Aibing Wu, Xuwei Yang, Hua Yang*

College of Chemistry, Jilin University, Changchun 130012, China

ARTICLE INFO

Article history:
Received 31 August 2011
Received in revised form 3 October 2011
Accepted 7 October 2011
Available online 17 October 2011

Keywords:
Fe@C
Co@C
Ni@C
Magnetic properties
Nanoparticles

ABSTRACT

Carbon coated Fe, Co and Ni nanoparticles (Fe@C, Co@C and Ni@C) have been fabricated by an efficient solid-state route using melamine as carbon source. The structure and morphology of Fe@C, Co@C and Ni@C nanoparticles were characterized by X-ray diffraction (XRD) and transmission electron microscopy (TEM). It is shown that the structure and morphology of Fe@C are different from those of Co@C and Ni@C. The crystallinity of carbon in Fe@C, Co@C and Ni@C nanoparticles was examined by Raman spectroscopy. The results indicate that the graphitization degree of carbon decreases in the order Fe@C > Co@C > Ni@C. Additionally, the reactions involved in the syntheses are speculated. The magnetic properties of Fe@C, Co@C and Ni@C nanoparticles were tested by VSM at room temperature. The variations of magnetic properties of Co@C and Ni@C with the increase of reactive temperatures are discussed respectively.

1. Introduction

Ferromagnetic nanoparticles have unique electric, optical and magnetic [1,2] properties that make them of potential use in various applications such as photocopying [3], medical imaging [4], magnetic drug targeting and magnetic hyperthermia [5,6]. Unfortunately, bare nanoparticles of ferromagnetic metals of iron group (Fe, Co, and Ni) are prone to rapid environmental degradation because of their high surface area to volume ratio and high reactivity. This drawback restricts their practical applications and even makes investigations of their nanocrystalline properties difficult [7–10]. One way to protect metal nanoparticles is to encapsulate the particles with a chemically stable species, such as graphite. Carbon is one of the best solutions for encapsulation as it is light, cheap and highly stable under extreme chemical and physical environments. The carbon coatings immunize the nanoparticles against environmental degradation and therefore retain their intrinsic nanocrystalline properties. Furthermore, carbon coatings can endow these nanoparticles with biocompatibility and a clear potential for further functionalization [11]. It is enormously significant for prospective biomedical applications [12].

Carbon-encapsulated magnetic nanoparticles (CEMNPs) have attracted great interest on account of their important applications in magnetic data storage, ferrofluids, biosensor, drug delivery and magnetic contract reagents [13–16]. Among the many types of CEMNPs with different core materials, those with iron group metals are in the center of interest, not only because these metals exhibit ferromagnetism at room temperature, but also because they have a unique catalyzing ability to transform amorphous carbon into graphite [17,18]. The synthesis routes of CEMNPs involve various methods, such as arc discharge [13], microwave heating [19], thermal plasma [20], explosion [21], chemical vapor condensation [22], and hydrothermal reaction [23]. Most of these methods, however, involve high energy consumption and require sophisticated apparatus, which typically leads to complicated operation and high costs in terms of practical applications.

In this work, we report a simple and economic method of synthesizing CEMNPs based on the pyrolysis of an organic compound melamine. The Melamine is an important raw material such as in the syntheses of flame-retardant thermoplastic polyester and of fireproof materials [24]. It has been reported that melamine can be used both as nitridation reagent [25] and carburization reagent [26]. The melamine is as carbon source for fabricating carbon-encapsulated Fe, Co and Ni nanoparticles respectively. The hydrothermally prepared nanocrystalline Fe/Fe_3O_4, Co_3O_4 and NiO, respectively, are used as corresponding metal precursor. The structure, morphology and graphitization degree of the nanocomposites are investigated. The effects of reactive temperature on the magnetic properties of carbon-encapsulated Co and Ni nanoparticles are discussed respectively.

2. Experimental

2.1. Preparation of metal precursors

All chemicals used are of analytical grade from commercial sources. The Fe/Fe_3O_4 nanocomposites were prepared by the hydrothermal method. Typically, 15 mmol ferrous chloride ($FeCl_2 \cdot 4H_2O$) was dissolved in 40 mL KOH aqueous

---

* Corresponding author.
E-mail address: huayang86@sina.com (H. Yang).

0925-8388/$ – see front matter © 2011 Elsevier B.V. All rights reserved.
doi:10.1016/j.jallcom.2011.10.018

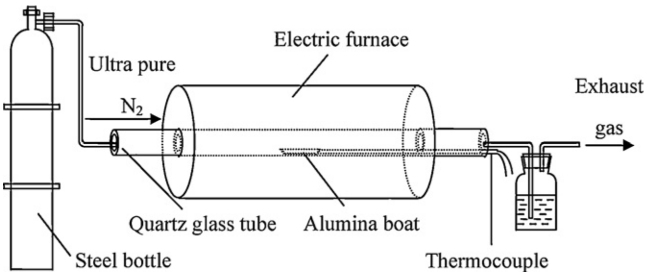

Fig. 1. Schematic of synthesis process.

solution (1 mol/L) under flowing nitrogen with magnetic stirring for 30 min. Then the reaction mixture was transferred into a Teflon-lined stainless steel autoclave with capacity of 50 mL, which was subsequently sealed and maintained at 180 °C for 18 h. After the autoclave was naturally cooled to room temperature, the resulting powder was centrifuged, washed with distilled water and ethanol for four times. The precipitate was dried in a vacuum oven at 60 °C for 6 h.

The Co_3O_4 and NiO nanoparticles were prepared by the hydrothermal method using $CoCl_2{\cdot}6H_2O$ and $NiCl_2{\cdot}6H_2O$ respectively, then were annealed at 400 °C for 2 h in air.

2.2. Synthesis of carbon-encapsulated Fe, Co, and Ni nanoparticles

The carbon-encapsulated Fe, Co and Ni nanoparticles were synthesized by solid-state reaction at atmospheric pressure. The metal precursor (MP) of Fe/Fe_3O_4, Co_3O_4 and NiO were mixed with the melamine at various molar ratios, then grounded with an agate mortar and pestle for 20 min to reduce agglomerations, crush large particles and increase contact between the carbon source and MP powder. In a typical synthesis, the ground powder with a predetermined molar ratio of melamine to MP was put in an alumina boat and then the boat was loaded into a quartz glass tube. The tube was placed into a horizontal electric tube furnace with the boat at the center of furnace. A thermocouple was inserted into the tube and kept very near to the boat to measure its exact temperature. Ultra pure nitrogen (purity; >99.999%) flow was introduced into the tube and after purging air for 10 min, the furnace was heated at a rate of 15 °C/min to required temperature and kept for a certain period of time. Finally the furnace power switch was turned off and the product was allowed to cool to room temperature while maintaining the flow of nitrogen. The nanocomposites were collected from the tube and once again ground up into a fine powder. The schematic of synthesis process is shown in Fig. 1.

2.3. Sample characterization

The X-ray powder diffraction (XRD) patterns were collected on a Shimadzu diffractometer with Cu Kα radiation ($\lambda = 0.15405$ nm). The transmission electron microscopy (TEM) and high-resolution transmission electron microscopy (HRTEM) images were obtained on a field-emission transmission electron microscope (TECNAI G2, 200 kV). The Raman spectra were recorded on a confocal Raman spectrometer (Renishaw-1000, UK) with 514 nm argon ion laser as excitation source. The room temperature magnetic hysteresis (*M*–*H*) loops were measured using a vibrating sample magnetometry (VSM) system (JDAM-2000D) with a maximum magnetic field of 10,000 Oe.

3. Results and discussion

3.1. Structure

Fig. 2A displays the XRD pattern of nanocrystalline Fe/Fe_3O_4 composite. It can be clearly seen that all the diffraction peaks, except the one at around $2\theta = 44.7^\circ$, can be perfectly indexed to face centered cubic (fcc) phase Fe_3O_4 (JCPDS card no. 88-0866) with a spinel structure and a space group of *Fd3 m*. The small peak at around $2\theta = 44.7^\circ$ can be assigned to body centered cubic (bcc) of Fe (JCPDS card no. 87-0722), indicating that there are Fe and Fe_3O_4 in the system.

Fig. 2B(a) shows the XRD pattern of as-prepared $Co(OH)_2$ nanoparticles by hydrothermal method at 180 °C for 18 h. All the diffraction peaks can be indexed to hexagonal phase of β-$Co(OH)_2$ (JCPDS card no. 30-0443). The XRD pattern of Co_3O_4 obtained by annealing $Co(OH)_2$ nanoparticles at 400 °C for 2 h in air is shown in Fig. 2B(b). It can be seen that all the diffraction peaks in this pattern can be well indexed to cubic phase of Co_3O_4 (JCPDS no. 74-1656). No other peaks of impurities are observed, indicating the complete transformation of $Co(OH)_2$ to Co_3O_4.

Fig. 2C(a) shows the XRD pattern of $Ni(OH)_2$ nanoparticles by hydrothermal method at 180 °C for 18 h. All the diffraction peaks can be indexed to hexagonal phase of β-$Ni(OH)_2$ (JCPDS card no. 14-0117). Fig. 2C(b) shows the XRD pattern of NiO obtained by annealing $Ni(OH)_2$ nanoparticles at 400 °C for 2 h in air. In this pattern, all the diffraction peaks match well with those of cubic phase of NiO (JCPDS card no. 71-1179). No other peaks of impurities are observed, indicating the complete transformation of $Ni(OH)_2$ to NiO.

The XRD patterns of Fe@C nanoparticles obtained at different reaction temperatures with molar ratio 4:1 of melamine and composite are shown in Fig. 3A. There are bcc-Fe and Fe_3C in Fig. 3A(a). There are Fe and a trace amount of Fe_3C in Fig. 3A(b). There are only bcc-Fe (JCPDS card no. 87-0722) in Fig. 3A(c), whose characteristic peaks are located at $2\theta = 44.7$ and 65.1°.

The XRD patterns of carbon-encapsulated Co nanoparticles obtained at different reaction temperatures with molar ratio 4:1 of melamine and Co_3O_4 are shown in Fig. 3B. All three XRD patterns at 2θ value of 44.4°, 51.6° and 76.0° are belong to the (1 1 1), (2 0 0) and (2 2 0) of face centered cubic Co (JCPDS card no. 89-4307). The XRD pattern of sample obtained at 650 °C exhibits two additional minor peaks at $2\theta = 42.0^\circ$ and 47.8° which are probably attributable to some unknown byproducts in Fig. 3B(a). The XRD patterns shown in Fig. 3B(a–c) are similar and both reveal a very weak and broad peak at around $2\theta = 26.4^\circ$ corresponding to the (0 0 2) diffraction plane of graphite. The XRD peak intensities of fcc-Co are increased with increasing temperature, which indicates the sample crystalline has been improved by increasing temperature.

The XRD patterns of carbon-encapsulated Ni nanoparticles obtained at different reaction temperatures with molar ratio 2:1 of melamine and NiO are shown in Fig. 3C. All three XRD patterns at 2θ value of 44.5°, 51.9° and 76.4° are corresponding to the (1 1 1), (2 0 0) and (2 2 0) of face centered cubic (fcc) Ni (JCPDS card no. 70-0989) in Fig. 3C. The XRD peak at around $2\theta = 26.4^\circ$ is corresponding to the (0 0 2) diffraction plane of graphite. The XRD peak intensity of fcc-Ni is decreased with increasing temperature, which is just opposite to the variation of that of fcc-Co. The XRD peak intensity of graphite is increased with increasing temperature.

3.2. Morphologies

Fig. 4(a) shows a typical low-magnification TEM image of carbon-encapsulated Fe nanoparticles obtained at 750 °C. It can be seen that the sample is composed of nanoparticles and nanosheets (indicated by the arrow). The nanoparticles are dispersed in the graphite nanosheets. A typical high-magnification TEM image of the sample shown in Fig. 4(b) reveals the particle size is in the range of 100–200 nm.

The TEM images of Co@C nanoparticles obtained at 750 °C are shown in Fig. 5. As can be seen in Fig. 5(a–c), the sample consists of carbon-encapsulated nanoparticles and carbon nanotubes (indicated by white arrows). Several nanoparticles trapped at the tips of carbon nanotubes can be observed in Fig. 5(b) (marked by white circles). Most of the nanoparticles are in the size range of 100–200 nm (Fig. 5(c)). A typical high-magnification image of the square region marked in Fig. 5(c) is shown in Fig. 5(d). It clearly reveals the core–shell structure of the carbon-encapsulated nanoparticle. Fig. 5(e) shows the HRTEM image of the square region in Fig. 5(d). The encapsulation is composed of a nanolayered material with interlayer distance of 0.34 nm [27] typical for the graphite (0 0 2) planes. The inter-lattice distance of the core is calculated to be 0.21 nm [28], which is consistent with that of fcc-Co (1 1 1) planes.

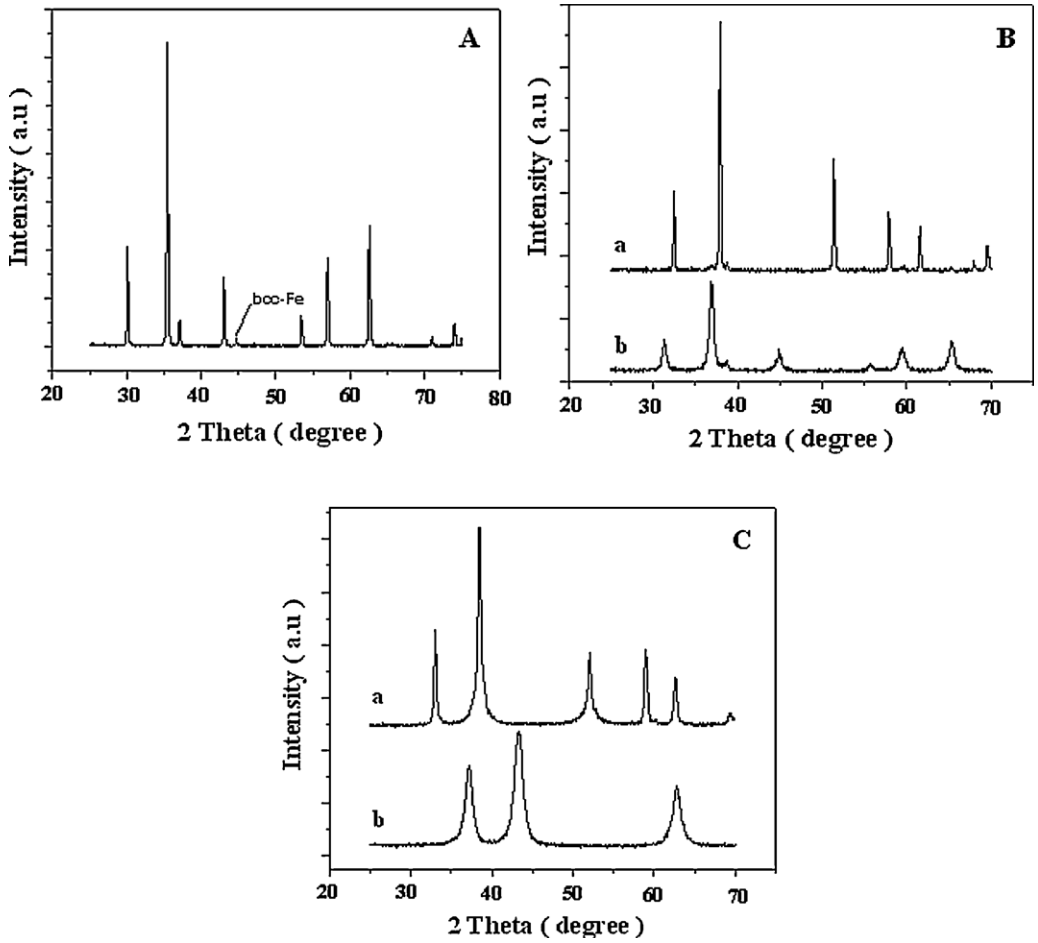

Fig. 2. XRD patterns of Fe/Fe_3O_4 (A); $Co(OH)_2$ (B) and $Ni(OH)_2$ (C) nanoparticles prepared at 180 °C for 18 h (a) and annealed at 400 °C for 2 h (b).

The TEM images of Ni@C nanoparticles obtained at 750 °C are shown in Fig. 6. It can be seen from Fig. 6(a) that the nanoparticles are spherical with sizes in the range of 30–60 nm. Fig. 6(b) displays well-defined core–shell structure of nanoparticles with shell thickness of about 20 nm. Fig. 6(c) shows a low-magnification image of the sample. A high-magnification image of a single nanoparticle in Fig. 6(c) is shown in Fig. 6(d). The HRTEM image of the square region in Fig. 6(d) is presented in Fig. 6(e). The interlayer distance of the encapsulation is 0.34 nm corresponding to graphite (0 0 2) planes. The inter-lattice distance of the core is 0.20 nm [29], which is in good agreement with that of fcc-Ni (1 1 1) planes.

3.3. Graphitization degree

Further information concerning the crystalline of the carbon phase was obtained from Raman spectroscopy. The Raman spectra of Fe@C nanoparticles obtained at 750 °C is shown in Fig. 7A. Two characteristic bands appear on the spectra: D and G located at ca. 1350 cm^{-1} and 1575 cm^{-1}, respectively. The disorder-induced D band is a consequence of carbon atom vibration (A_{1g} mode) of defective graphite lattice, disordered carbon particles or amorphous carbon [30]. The G band, characteristic of graphite, is attributed to the stretch vibration (E_{2g} mode) of sp^2-hybridized carbon atoms in the graphite layer [31,32]. The width of G band is proportional to the extent of disorder in the graphite [33]. The intensity of D band is disproportional to the average size of graphite particles [34]. Thus, the intensity ratio of G band to D band is a convenient indicator of the overall graphitization degree [35]. It can be seen from Fig. 7A that the G band is strong and sharp while the D band is weak and broad, which illustrates that the graphite in the sample is highly ordered and the average size of graphite-encapsulated nanoparticles is relatively large. According to the spectra, the G/D ratio is calculated to be 3.27 which reflects the high graphitization degree of the sample.

Fig. 7B shows the Raman spectra of Co@C nanoparticles obtained at 750 °C. D and G bands located at ca. 1350 cm^{-1} and 1575 cm^{-1}, respectively, can also be observed in the spectra. The two bands are broader than those in Fig. 7A and the G/D ratio is 1.34 lower than that for Fe counterparts, which indicates a relatively low graphitization degree of the sample and the presence of more defects and impurities. This result is consistent with that derived by TEM observations.

Fig. 7C shows the Raman spectra of Ni@C nanoparticles obtained at 750 °C. The two bands D and G at 1350 cm^{-1} and 1575 cm^{-1}, respectively, are broader than those in Fig. 7C. The calculated G/D ratio1.23 is lower than their Fe and Co counterparts. These results can be related to the findings obtained by TEM observations.

3.4. Chemical reactions involved

This route is considered to be modified solid-state metathesis (SSM) [36–39] pathway. The starting materials, melamine and metal precursors (Fe/Fe_3O_4, Co_3O_4 and NiO) are in the solid-state before the reactions. The melamine can be transformed into different intermediates and meanwhile release ammonia at different temperatures [40]. Several important intermediates such as melam ($(C_3N_3)_2(NH_2)_4(NH)$), melem ($C_6N_7(NH_2)_3$), melon ($(C_6N_7)_3(NH_2)_3(NH)_3$) and graphitic carbon nitride materials

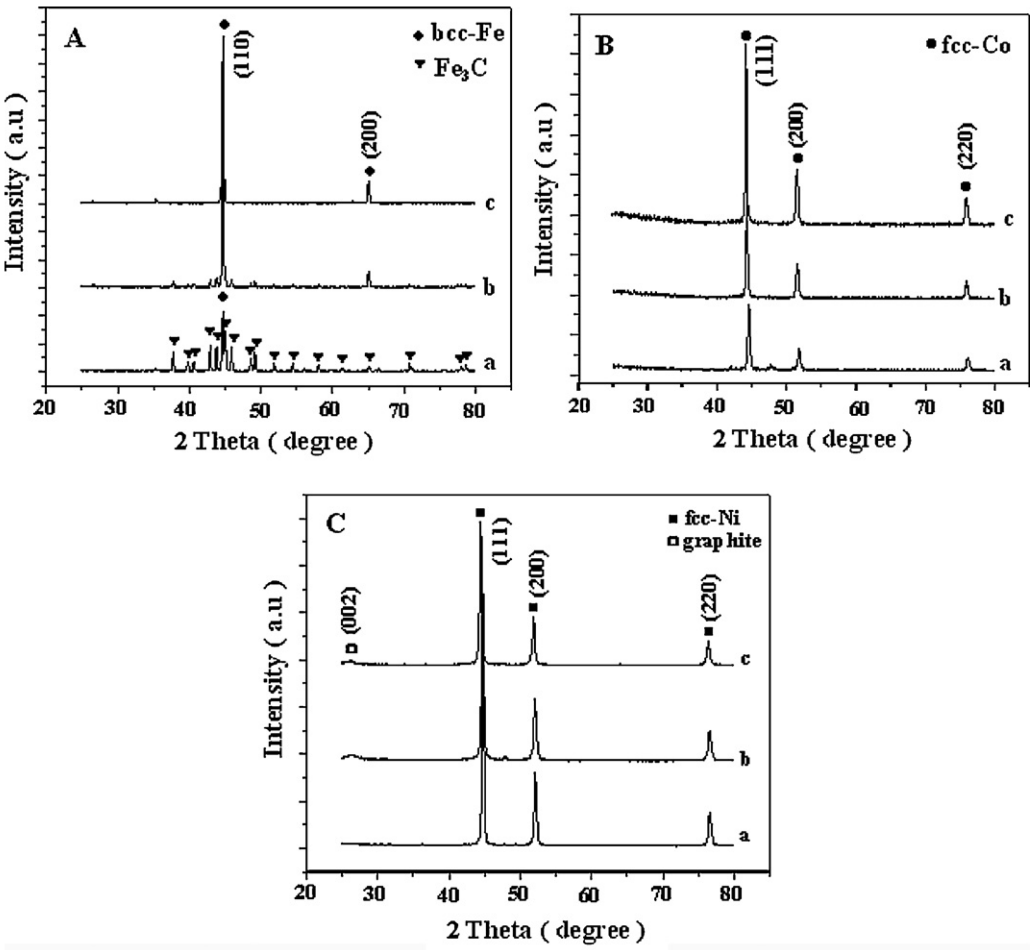

Fig. 3. XRD patterns of Fe@C (A), Co@C (B) and Ni@C (C) nanoparticles prepared at (a) 650 °C, (b) 700 °C and (c) 750 °C for 3 h.

(g-C_3N_4) can be formed with increasing temperature. Then, g-C_3N_4 can be decomposed into various carbon nitride species such as $C_3N_3^+$, $C_2N_2^+$, $C_3N_2^+$, and CN_2^+ over 600 °C [41–44]. These highly active species can firstly make metal oxide reduce into elemental metal. Finally, these metal atoms may further react with carbon nitride species to form metal carbide or metal nitride.

It is assumed that the thermal stability of metal carbides (e.g. Fe_3C, Co_3C and Ni_3C) is better than their corresponding nitride counterparts in the present temperature range 650–750 °C [45]. Thus metal carbides (e.g. Fe_3C, Co_3C and Ni_3C) may be produced by the chemical reaction between carbon, nitride species and elemental metals. In this study, when the reactive temperature is 650 °C, Fe and Fe_3C are formed from the chemical reaction between melamine and Fe/Fe_3O_4. The product obtained at 700 °C consists of Fe and a small quantity of Fe_3C, which can be ascribed to the decomposition of Fe_3C [46]. All of Fe_3C are decomposed to Fe and carbon to over 750 °C.

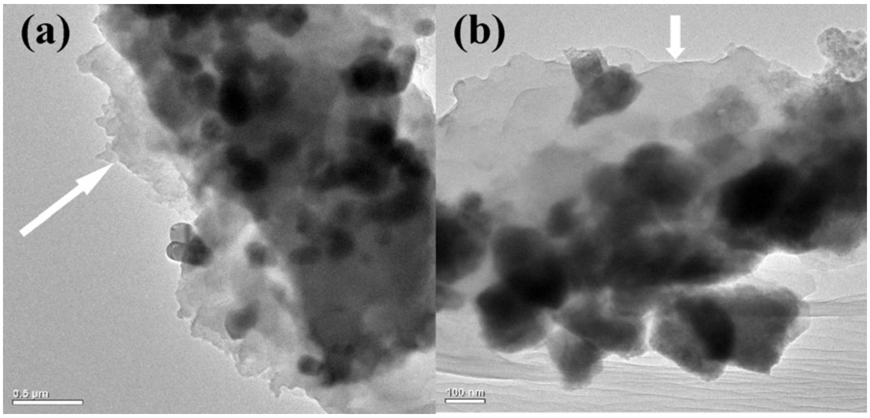

Fig. 4. TEM images of Fe@C nanoparticles obtained at 750 °C: (a) a low-magnification image and (b) a high-magnification image. The white arrows indicate the graphite nanosheets.

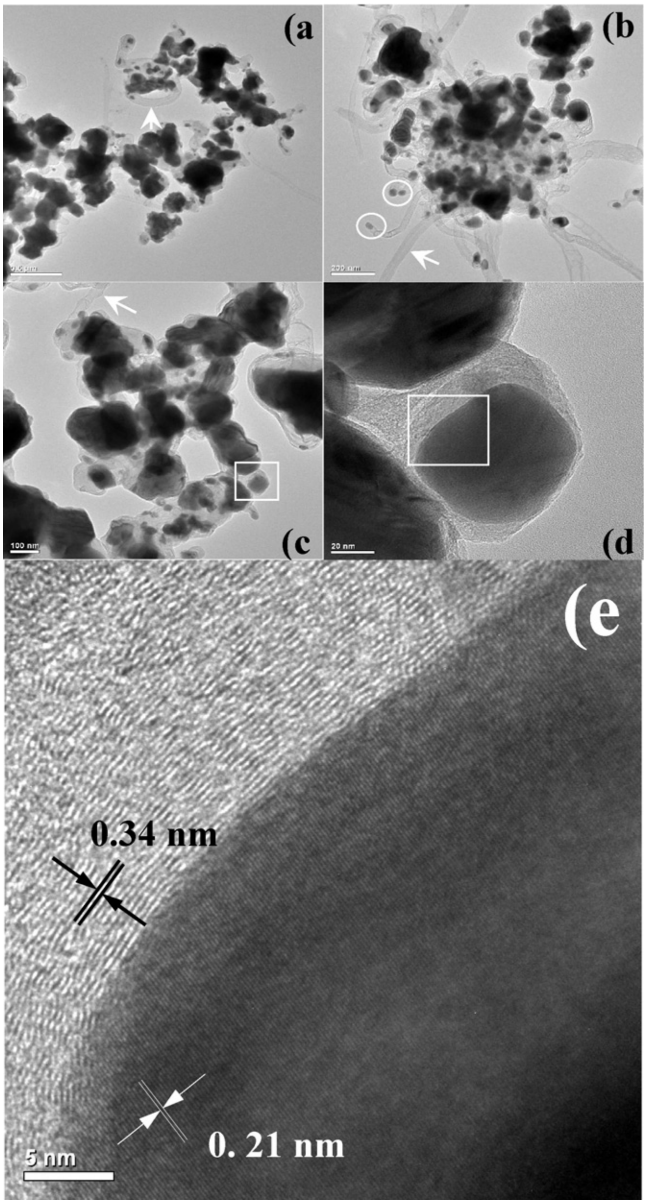

Fig. 5. TEM images of Co@C nanoparticles obtained at 750 °C: (a–c) low-magnification images showing coexistence of nanoparticles and nanotubes; (d) a high-magnification image of the square region marked in (c); (e) HRTEM image of the square region in (d).

The overall reactive processes can be speculated as follows:

$$C_3N_3(NH_2)_3 \xrightarrow{-NH_3} (C_3N_3)_2(NH_2)_4(NH) \xrightarrow{-NH_3} C_7N_7(NH_2)_3$$

$$C_6N_7(NH_2)_3 \xrightarrow{-NH_3} (C_6N_7)_3(NH_2)_3(NH)_3 \xrightarrow{-NH_3} g\text{-}C_3N_4$$

$$4C_3N_4 + 3Fe_3O_4 \rightarrow 9Fe + 8N_2 + 12CO$$

$$C_3N_4 + 9Fe \rightarrow 3Fe_3C + 2N_2$$

$$Fe_3C \rightarrow 3Fe + C$$

For the reactions between the melamine and metal oxide (Co_3O_4 or NiO), there are no carbide (Co_3C or Ni_3C) at 650–750 °C. It is reported that the stability of carbides is decreased in the order $Fe_3C > Co_3C > Ni_3C$ [47]. The decomposition temperatures of Co_3C and Ni_3C are around 500 °C [48] and 400 °C [49], respectively, which are both lower than 650 °C.

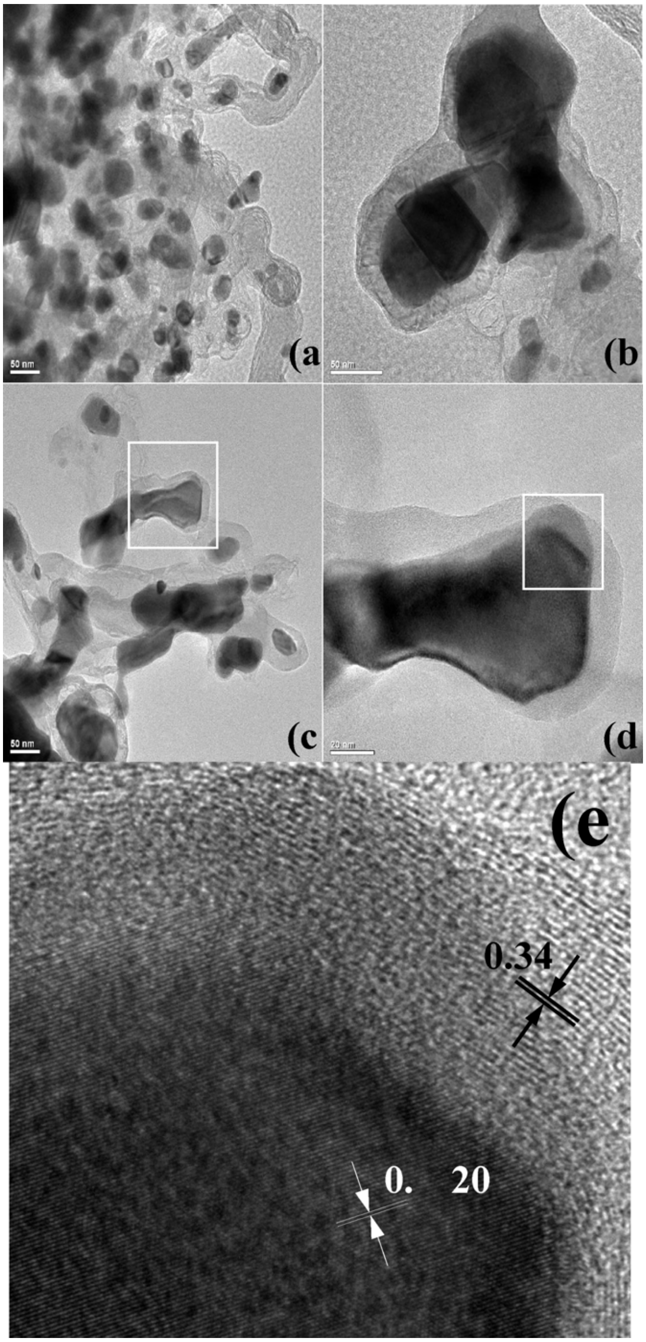

Fig. 6. TEM images of Ni@C nanoparticles obtained at 750 °C: (a–c) low-magnification images; (d) a high-magnification image of the square region marked in (c); (e) HRTEM image of the square region in (d).

The formation reactions of elemental metals Co and Ni are:

$$4C_3N_4 + 3Co_3O_4 \rightarrow 9Co + 8N_2 + 12CO$$

$$C_3N_4 + 3NiO \rightarrow 3Ni + 2N_2 + 3CO$$

3.5. Magnetic properties

The magnetic properties of the nanoparticles are investigated by VSM at room temperature. Fig. 8A presents the magnetization curve of Fe@C nanoparticles obtained at 750 °C, which is denoted as

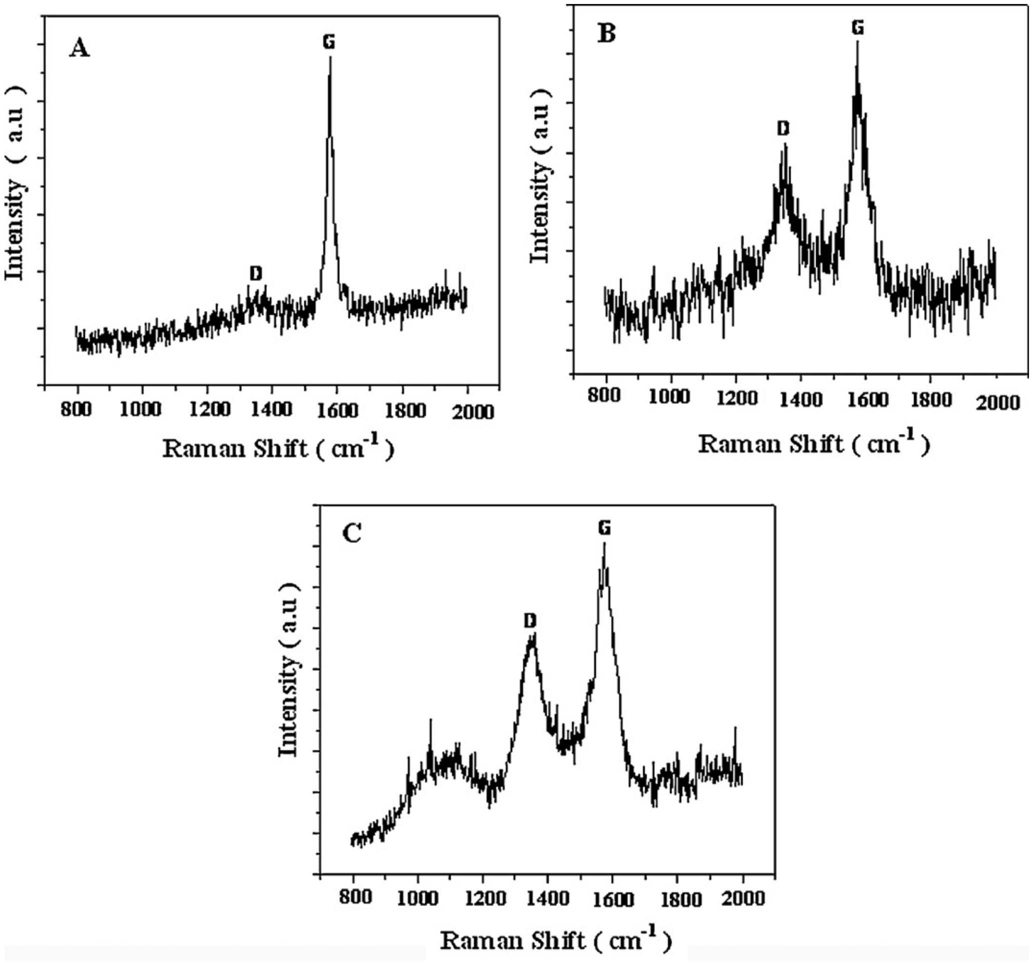

Fig. 7. Raman spectra of Fe @C (A), Co@C (B) and Ni@C (C) nanoparticles at 750 °C.

Fe@C-750. It is shown that the Fe@C nanoparticles have ferromagnetic behaviors. Its special saturation magnetization M_S is 198 emu/g, which is slightly smaller than the value 212 emu/g of bulk Fe [50]. Its coercivity is as small as about 66 Oe.

Fig. 8B shows the magnetization curves of Co@C nanoparticles obtained at different temperatures, which are denoted as Co@C-650, Co@C-700 and Co@C-750. These materials all exhibit ferromagnetic behavior at room temperature. They all exhibit larger hysteresis loops than that of Fe counterparts. Their special saturation magnetization M_S and coercivity H_C are listed in Table 1. It is found that the M_S and H_C vary with increasing temperature in the opposite direction. Among the three samples, Co@C-650 has the highest M_S 132 emu/g, which is slightly smaller than the value 162 emu/g of bulk Co [51]. Co@C-700 has the lowest magnetization and highest coercivity. Co@C-750 has a higher magnetization 125 emu/g, which is smaller than that of Co@C-650. The variations of magnetic properties can be attributed to the changes of crystallinity of Co@C. For Co@C nanoparticles with relatively large sizes (100–200 nm), the crystallinity of both the Co as the cores and carbon as the shells are increased with increasing temperature (see above Fig. 3B). It is assumed that the magnetic properties of core-shell nanostructures are depend mainly on the non-magnetic carbon shells below the temperature of 700 °C. Therefore, the increase of crystallinity of carbon as shells is caused a deterioration of magnetic properties. When the graphitic carbon reaches a certain degree of crystallization over 700 °C, the ferromagnetic Co cores play a major role in the magnetic properties. The increase of crystallinity of Co as cores is caused an improvement of magnetic properties.

Table 1
Magnetic properties of Co@C and Ni@C nanoparticles at different temperatures.

Sample	Temperature (°C)	M_S (emu/g)	H_C (Oe)
Co@C-650	650	132	187
Ni@C-650		48.5	180
Co@C-700	700	118	234
Ni@C-700		36.4	205
Co@C-750	750	125	226
Ni@C-750		33.8	206

Fig. 8C shows the magnetization curves of Ni@C nanoparticles obtained at different temperatures. The samples are denoted as Ni@C-650, Ni@C-700 and Ni@C-750. They also exhibit distinct hysteresis loops and ferromagnetic behavior at room temperature in Table 1. The Ni@C-650 nanoparticles has the highest magnetization and lowest coercivity, which M_S 48.5 emu/g is slightly smaller than the value 55.4 emu/g of bulk Ni [52]. It is found that M_S is decreased with increasing temperature, while H_C is increased. For Ni@C nanoparticles with relatively small sizes (30–60 nm), the crystallinity of carbon shells is increased with increasing temperature (see above Fig. 3B). It is assumed that the changes of crystallinity of carbon shells in the temperature range 650–750 °C make the main contribution to the variations of magnetic properties of Ni@C nanoparticles. Thus the increase of crystallinity of non-magnetic carbon shells is caused a deterioration of magnetic properties.

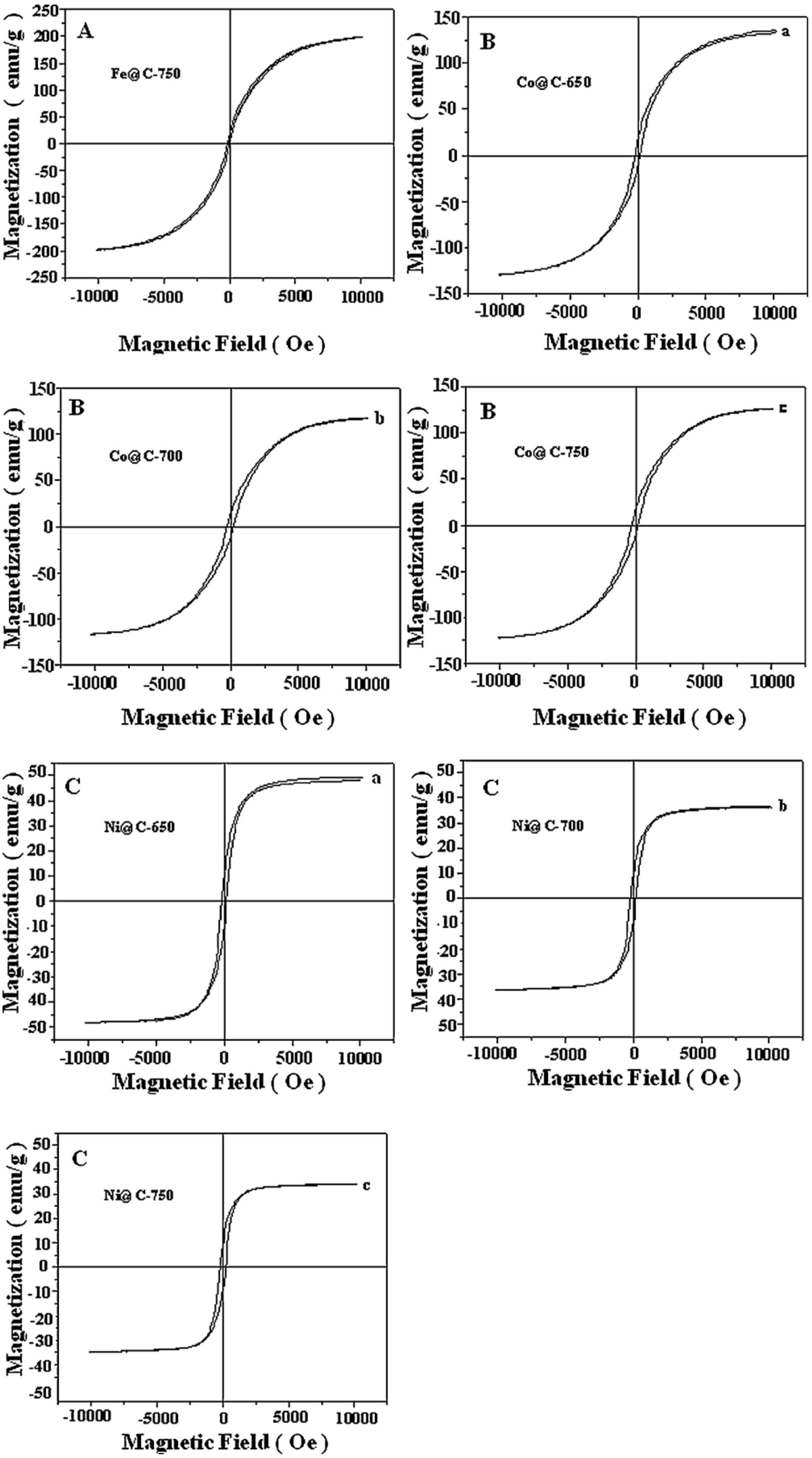

Fig. 8. Magnetization curves of Fe@C (A) nanoparticles at 750 °C, Co@C (B) and Ni@C (C) nanoparticles at (a) 650 °C, (b) 700 and (c) 750 °C.

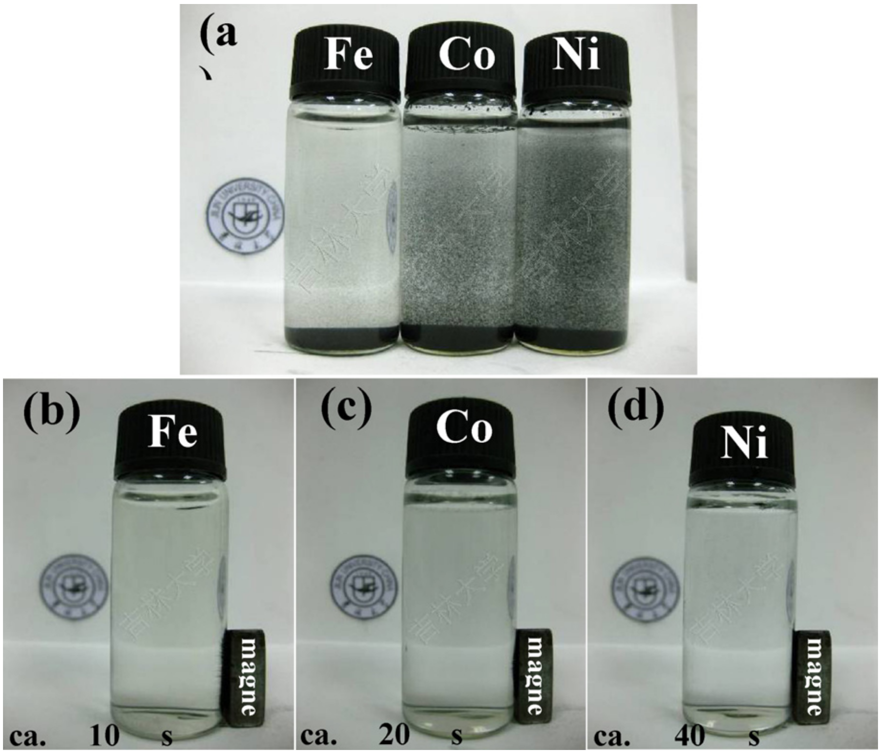

Fig. 9. Digital photographs of aqueous dispersions of M@C-750 (M = Fe, Co, Ni) nanoparticles under different conditions: (a) let stand for 10 s after ultrasonication; (b–d) in a magnetic field applied on one side.

Fig. 9 shows the digital photographs of aqueous dispersions of Me@C-750 (Me = Fe, Co, Ni) nanoparticles. Fig. 9(a) represents the photograph of the three dispersions after ultrasonication without applied magnetic field. It can be seen that the dispersions reflect different degrees of darkness. The degree of darkness of Fe@C-750 dispersion is lowest, while that of Ni@C-750 dispersion is highest. This phenomenon is mainly attributed to different average particle sizes of three samples. Fig. 9(b)–(d) displays the photographs of the three dispersions under applied magnetic field. The three samples are almost completely attracted to the side of the magnet after different times. Fe@C-750 is shown to fastest response to the applied magnetic field, while Ni@C-750 is shown to lowest response. This is a consequence of differences in magnetic properties of the samples.

4. Conclusions

We have developed a new approach to solid-state synthesis of carbon-encapsulated magnetic nanoparticles using melamine as carbon source. Fe@C, Co@C and Ni@C nanoparticles were synthesized throng the reactions of the melamine with nanocrystalline Fe/Fe$_3$O$_4$, Co$_3$O$_4$ and NiO, respectively. Fe@C is synthesized at 750 °C, while Co@C and Ni@C were synthesized in the range of 650–750 °C. Fe@C nanoparticles with diameters 100–200 nm are dispersed in several graphite nanosheets. The Co@C-750 and Ni@C-750 with diameter ranges 100–200 nm and 30–60 nm, respectively, are coated with graphite nanolayers. Furthermore, the crystallinity of carbon in the three nanoparticles were examined by Raman spectroscopy. It is shown that carbons mostly are located in the form of graphite and the graphitization degree of carbon is decreased in the order Fe@C > Co@C > Ni@C. Magnetic measurements reveal that the synthesized materials all exhibit ferromagnetism at room temperature. Fe@C-750 has a special saturation magnetization M_S (198 emu/g) close to that of bulk Fe. Co@C-650 and Ni@C-650 have maximum special saturation magnetizations M_S of 132 emu/g and 48.5 emu/g, respectively, which are slightly smaller than the ones of bulk materials. Considering the simplicity of the experimental apparatus, the wide availability of melamine and good reproducibility, the present approach has a potential for synthesis of other carbon-encapsulated nanoparticles and nanomaterials.

Acknowledgement

This work is supported by the National Natural Science Foundation of China.

References

[1] R.H. Kodama, J. Magn. Magn. Mater. 200 (1999) 359–372.
[2] A. Fert, L. Piraux, J. Magn. Magn. Mater. 200 (1999) 338–358.
[3] C.B. Duke, J. Noolandi, T. Thieret, Surf. Sci. 500 (2002) 1005–1023.
[4] T.J. Senden, K.H. Moock, J.F. Gerald, W.M. Burch, R.J. Browitt, Ch.D. Ling, G.A. Heath, J. Nucl. Med. 38 (1997) 1327–1333.
[5] A.J. Almeida, S. Runge, R.H. Muller, Int. J. Pharm. 149 (1997) 255–265.
[6] U. Sarı, T. Kırındı, M. Yüksel, S. Ağan, J. Alloy Compd. 476 (2009) 160–163.
[7] D.L. Peng, Y. Chen, H. She, R. Katoh, K. Sumiyama, J. Alloy Compd. 469 (2009) 276–281.
[8] J.-H. Hwang, V.P. Draid, M.H. Teng, J.J. Host, B.R. Elliott, D.L. Johnson, T.O. Mason, J. Mater. Res. 12 (1997) 1076–1082.
[9] J.J. Host, J.A. Block, K. Parvin, V.P. Dravid, J.L. Alpers, T. Sezen, R. LaDuca, J. Appl. Phys. 83 (1998) 793–801.
[10] G. Cui, Y.-S. Hu, L. Zhi, D. Wu, I. Lieberwirth, J. Maier, K. M€ullen, Small 3 (2007) 2066–2069.
[11] Y.W. Ma, Z. Hu, L.S. Yu, Y.M. Hu, B. Yue, X.Z. Wang, Y. Chen, J. Phys. Chem. B 110 (2006) 20118–20122.
[12] P. Gould, Mater. Today 2 (2004) 36–41.
[13] J.H. Scott, S.A. Majetich, Phys. Rev. B 52 (1995) 12564–12571.
[14] M.E. McHenry, S.A. Majetich, J.O. Artman, M. DeGraef, Phys. Rev. B 49 (1994) 11358–11363.
[15] A.A. Bogdanov, C. Martin, R. Weissleder, Biochim. Biophys. Acta 1193 (1994) 212–218.
[16] S. Pauser, R. Reszka, S. Wagner, Anti-Cancer Drug Des. 112 (1997) 125–135.
[17] J.J. Host, M.H. Teng, B.R. Elliott, J.-H. Hwang, T.O. Mason, J.R. Weertman, D.L. Johnson, V.P. Dravid, J. Mater. Res. 12 (1997) 1268–1273.
[18] B.R. Elliott, J.J. Host, V.P. Dravid, M.H. Teng, J.-H. Hwang, J. Mater. Res. 12 (1997) 3328–3344.
[19] D.S. Jacob, I. Genish, L. Klein, A. Gedanken, J. Phys. Chem. B 110 (2006) 17711–17714.

[20] M. Bystrzejewski, A. Huczko, H. Lange, P. Baranowski, G. Cota-Sanchez, G. Soucy, J. Szczytko, A. Twardowski, Nanotechnology 18 (2007) 145608.

[21] W.Z. Wu, Z.P. Zhu, Z.Y. Liu, Y.N. Xie, J. Zhang, T.D. Hu, Carbon 41 (2003) 317–321.

[22] Z.H. Wang, Z.D. Zhang, C.J. Choi, B.K. Kim, J. Alloy. Compd. 361 (2003) 289–293.

[23] Z.F. Wang, P.F. Xiao, N.Y. He, Carbon 44 (2006) 3277–3284.

[24] N. Kimizuka, T. Kawasaki, K. Hirata, T. Kunitake, J. Am. Chem. Soc. 117 (1995) 6360–6361.

[25] H.Z. Zhao, M. Lei, X.L. Chen, W.H. Tang, J. Mater. Chem. 16 (2006) 4407–4412.

[26] M. Lei, H.Z. Zhao, H. Yang, B. Song, W.H. Tang, J. Eur. Ceram. Soc. 28 (2008) 1671–1677.

[27] H.P. Li, N.Q. Zhao, C.N. He, C.S. Shi, X.W. Du, J.J. Li, J. Alloy Compd. 458 (2008) 130–133.

[28] S.V. Pol, V.G. Pol, G. Seisenbaeva, V.G. Kessler, A. Gedanken, Chem. Mater. 16 (2004) 1793–1798.

[29] J.H. Byeon, J.H. Park, K.Y. Yoon, J. Hwang, Nanoscale 1 (2009) 339–343.

[30] V. Datsyuk, M. Kalyva, K. Papagelis, J. Parthenios, D. Tasis, A. Siokou, I. Kallitsis, C. Galiotis, Carbon 46 (2008) 833–840.

[31] W.M. Zhu, J.W. Ren, X. Gu, M.U. Azmat, G.Z. Lu, Y.Q. Wang, Carbon 49 (2011) 1462–1472.

[32] E.B. Barros, N.S. Demir, A.G. Souza Filho, J.M. Filho, A. Jorio, G. Dresselhaus, M.S. Dresselhaus, Phys. Rev. B 71 (2005) 165422.

[33] M. Bystrzejewski, Z. Karoly, J. Szepvolgyi, W. Kaszuwara, A. Huczko, H. Lange, Carbon 47 (2009) 2040–2048.

[34] S.M. Huang, Z. Sun, Y.F. Lu, M.H. Hong, Surf. Coat. Technol. 151–152 (2002) 263–267.

[35] K. Shen, S. Curran, H.F. Xu, S. Rogelj, Y.B. Jiang, J. Dewald, T. Pietrass, J. Phys. Chem. B 109 (2005) 4455–4463.

[36] A.M. Nartowski, I.P. Parkin, A.J. Craven, M. MacKenzie, Adv. Mater. 10 (1998) 805–808.

[37] A.M. Nartowski, I.P. Parkin, M. MacKenzie, A.J. Craven, J. Mater. Chem. 11 (2001) 3116–3119.

[38] J.B. Wiley, R.B. Kaner, Science 255 (1992) 1093–1097.

[39] E.G. Gillan, R.B. Kaner, Chem. Mater. 8 (1996) 333–343.

[40] B. Jurgens, E. Irran, J. Senker, H. Muller, W. Schnick, J. Am. Chem. Soc. 125 (2003) 10288–10300.

[41] V.N. Khabashesku, J.L. Zimmerman, J.L. Margrave, Chem. Mater. 12 (2000) 3264–3270.

[42] E.G. Gillan, Chem. Mater. 12 (2000) 3906–3912.

[43] B.V. Lotsch, W. Schnick, Chem. Mater. 17 (2005) 3976–3982.

[44] H.Z. Zhao, M. Lei, X.A. Yang, J.K. Jian, X.L. Chen, J. Am. Chem. Soc. 127 (2005) 15722–15723.

[45] S. van Dommele, A. Romero-Izquirdo, R. Brydson, K.P. de Jong, J.H. Bitter, Carbon 46 (2008) 138–148.

[46] A.B. Wu, D.M. Liu, L.Z. Tong, L.X. Yu, H. Yang, CrystEngComm 13 (2011) 876–882.

[47] O.P. Krivoruchko, V.I. Zaikovskii, Mendeleev. Commun. 8 (1998) 97–99.

[48] S. Nagakura, J. Phys. Soc. Jpn. 12 (1957) 482–494.

[49] S. Nagakura, J. Phys. Soc. Jpn. 16 (1961) 1213–1219.

[50] Y. Leconte, S. Veintemillas-Verdaguer, M.P. Morales, R. Costo, I. Rodríguez, P. Bonville, B. Bouchet-Fabre, N. Herlin-Boime, J. Colloid Interface Sci. 313 (2007) 511–518.

[51] C.W. Kim, H.G. Cha, Y.H. Kim, A.P. Jadhav, E.S. Ji, D.I. Kang, Y.S. Kang, J. Phys. Chem. C 113 (2009) 5081–5086.

[52] E.P. Wohlfarth, Ferromagnetic Materials, North-Holland, Amsterdam, 1980, pp. 1–20.